Ferroelectric control of the Néel vector in *L*10-type antiferromagnetic films

Fanxing Zheng, Meng Zhu, Xinlu Li, Peina Zhang, Jiuzhao Liu, Jianting Dong, and Jia Zhang*
School of Physics and Wuhan National High Magnetic Field Center, Huazhong University of Science and Technology, 430074 Wuhan, China

(Received 7 February 2021; revised 18 September 2021; accepted 20 September 2021; published 4 October 2021)

How to efficiently manipulate the Néel vector of antiferromagnets by electric methods is one of the major focuses in current antiferromagnetic spintronics. In this work, we investigated the ferroelectric control of magnetism in antiferromagnetic *L*10-MnPt/$BaTiO_3$ bilayer structures by using first-principles calculation. We studied the effect of ferroelectric polarization reversal on magnetic crystalline anisotropy (MCA) of *L*10-MnPt films with different interface structures. Our results predict a large perpendicular MCA in *L*10-MnPt films with Pt-O interface, and an in-plane MCA with Mn-O interface when they are interfaced with ferroelectric $BaTiO_3$. In addition, the magnitude of MCA for both interfaces can be modulated efficiently by the polarization reversal of $BaTiO_3$. The ferroelectric control of MCA has been analyzed based on second order perturbation theory, and it can be mainly attributed to the ferroelectric polarization driven redistribution of Pt-5*d* orbital occupation around Fermi energy. Especially, for the Mn-O interface, the Néel vector can be switched between in-plane [100] and [110] directions, or even from in plane to out of plane at certain film thickness by reversing ferroelectric polarization. Our results may provide a nonvolatile concept for ferroelectric control of Néel vector in *L*10 antiferromagnets, which could stimulate experimental investigations on magnetoelectric effect of antiferromagnets and promote its applications in low-power consumption spintronic memory devices.

DOI: 10.1103/PhysRevB.104.144403

I. INTRODUCTION

Recently, electric control of antiferromagnetic states has been widely discussed and investigated [1–3]. Compared with ferromagnetic (FM) materials, antiferromagnetic (AFM) materials are robust against external magnetic field, produce no stray field, and exhibit ultrafast dynamics [2,4]. Those features make AFM materials appealing for applications in nonvolatile memory [5,6]. However, how to efficiently manipulate the magnetic states of AFM materials by electric means is one of the key issues for future development of AFM materials based spintronics devices.

Currently, intensive research attention has been focused on the electric current switching of AFM states [7–9]. A number of theoretical and experimental works have demonstrated that in several AFM materials like Mn_2Au, CuMnAs with specific crystal symmetry [10–12], and in AFM/heavy metal bilayer structures [13–15], the electric current can manipulate the Néel vector in AFM materials through a spin-orbit torque (SOT) mechanism [16]. Unfortunately, in order to manipulate the antiferromagnetic state, a current density typically around 10^6–10^7 A/cm^2 is required [9,17,18]. Therefore, a more energy efficient switching mechanism is necessary for manipulating antiferromagnetic states [19–21].

Instead of using electric current, an alternative promising approach to manipulate Néel vector of AFM materials may be applying electric field [22,23]. In the antiferroelectric/ferroelectric bilayers structure, ferroelectric polarization can be reversed by applying electric field, so as to possibly manipulate the magnetic properties of adjacent AFM films. Earlier theoretical calculations have predicted magnetoelectric effect in Fe/$BaTiO_3$ interface [24]. And in FeRh/$BaTiO_3$ bilayers, it has also been proved that a moderate electric field is sufficient to adjust the AFM-FM phase transition and magnetic crystalline anisotropy (MCA) of FeRh [25,26]. MnPt belongs to the *L*10 type of metallic AFM materials, which has high Néel temperature ($T_N = 970$ K) and makes it suitable for practical applications. In addition, previous first-principles calculations indicate that the easy axis of bulk *L*10-MnPt is along the *c* axis and is sensitive to the number of electrons [27]. Those properties stimulate our investigations on ferroelectric control of MCA in MnPt films.

In this work, we set up *L*10-MnPt/$BaTiO_3$ bilayers and investigate the ferroelectric control of MCA in MnPt films with various thickness by using first-principles calculations. As shown in Figs. 1(a) and 1(b), we consider two possible interface structures between MnPt and $BaTiO_3$, namely, Pt and Mn layers in MnPt that sit on top of O atoms in the TiO_2 plane of $BaTiO_3$. There is a small in-plane lattice mismatch (0.28%) between *L*10-MnPt ($a = b = 3.980$ Å, $c = 3.720$ Å) [28] and $BaTiO_3$ ($a = b = 3.991$ Å, $c = 4.035$ Å) [29], which suggests the proposed *L*10-MnPt/$BaTiO_3$ bilayer structures could be experimentally achievable. The calculation results demonstrate that for Pt-O interface, MnPt films have a large perpendicular magnetic anisotropy (PMA) high up to several mJ/m^2 (hereafter the MCA is defined as the total MCA energy of film in the unit cell divided by the unit cell area, which means the MCA of the films per unit area), while for Mn-O interface, the magnetic easy axis of MnPt keeps in plane in the studied film thickness. Importantly, our results prove the concept that, instead of electric current, the reversal of

*jiazhang@hust.edu.cn

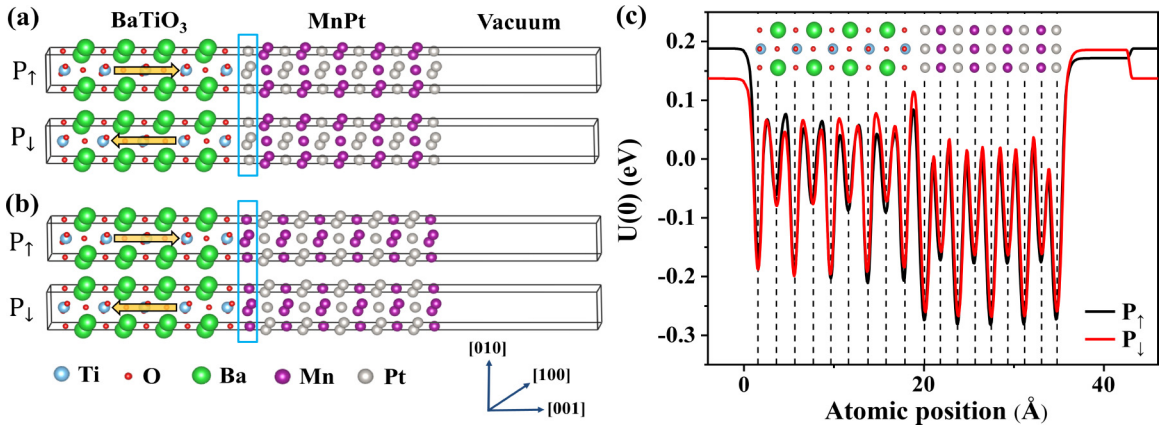

FIG. 1. The side view of MnPt (4 u.c.)/$BaTiO_3$ (4 u.c.)/vacuum structures with Pt-O (a) and Mn-O (b) interfaces for $P_\uparrow$ and $P_\downarrow$ ferroelectric polarization states. The light blue squares highlight the interfacial layers of $L1_0$-MnPt films. Yellow arrows indicate the directions of ferroelectric polarization. The crystal coordinate axes are also indicated in the bottom right corner. (c) The planar averaged electrostatic potential energy distribution in MnPt (4 u.c.)/$BaTiO_3$ (4 u.c.)/vacuum structure for $P_\uparrow$ (black line) and $P_\downarrow$ (red line) polarization states.

ferroelectric polarization could remarkably modify the magnitude of MCA in adjacent AFM thin films. What's more, for the Mn-O interface case, the Néel vector orientations of MnPt films can be realized by reversing ferroelectric polarization of $BaTiO_3$.

II. CALCULATION METHODS

The first-principles calculations are performed by employing the projector augmented wave (PAW) pseudopotential [30] and the Perdew-Burke-Ernzerhof (PBE) type of generalized gradient approximation (GGA) for the exchange correlation potential [31] as implemented in the Vienna *ab initio* simulation package (VASP) [32]. The $L1_0$-MnPt/$BaTiO_3$ bilayers are modeled by using a supercell with the vacuum thickness of no less than 15 Å as it is shown in Fig. 1(a). The thickness of MnPt films is varied from one to five unit cells (1–5 u.c.), while the thickness of $BaTiO_3$ is fixed to be 4 u.c. which is proved to be sufficient for establishing its ferroelectric stability [33]. The in-plane lattice constant of the supercell is fixed to be the bulk value of $BaTiO_3$ (3.991 Å). The dipole correction is applied in order to minimize the artificial electrostatic interactions between asymmetric surface layers [34]. As shown in Fig. 1(c), the step of electrostatic potential appears in vacuum region due to dipole correction, which eliminates the artificial electric field across the neighboring supercell.

An energy cutoff of 500 eV and $12 \times 12 \times 1$ k-point mesh in the Brillouin zone are used for structure relaxation until the force on each atom is less than 10 meV/Å. During the relaxations of ionic positions, MnPt atoms are allowed to fully relax, while only one unit cell of $BaTiO_3$ on the interface is allowed to relax, and the other three unit cells of $BaTiO_3$ away from MnPt-$BaTiO_3$ interface are fixed to their bulk positions. The $P_\uparrow$ and $P_\downarrow$ represent the Ti atoms displacement toward and away from MnPt interface as shown in Fig. 1(a). By calculating the interface binding energy, the Mn-O interface may be more stable in comparison to the Pt-O interface (see Appendix A). However, experimentally, both interface structures might be fabricated by depositing monolayer Pt or Mn before preparing MnPt films. The interface magnetic states (FM or AFM) have also been investigated in Appendix B, which indicate that the reversal of the ferroelectric polarization does not change the interface AFM order both for Mn-O and Pt-O interface structures.

The MCA is calculated based on the force theorem. First, a self-consistent calculation in the absence of spin-orbit coupling (SOC) is performed to obtain charge density by using $24 \times 24 \times 1$ k points. Then, the MCA is evaluated by using a much denser k-point mesh of $35 \times 35 \times 1$ which has been checked for convergence. The MCA is obtained by taking the band energy difference for magnetization along in-plane and out-of-plane directions as MCA $= E_{\text{band}}[abc]$-$E_{\text{band}}[001]$, where $[abc]$ indicates that the Néel vector is along in-plane [100] or [110] directions.

The Néel vector orientations of MnPt films are determined by the total magnetic anisotropy energy (MAE $=$ MCA $+ M_{dd}$) which includes MCA as well as the magnetic dipole-dipole anisotropy energy (M_{dd}). However, M_{dd} originating from magnetostatic interaction of magnetic moments has not been included in the first-principles calculations [35]. We explicitly calculate M_{dd} of MnPt films by employing real-space summation as described in Appendix C.

III. RESULTS AND DISCUSSION

As shown in Figs. 2(a) and 2(c), one can observe that the MCA is large and typically around several mJ/m^2 in MnPt films by interfacing with $BaTiO_3$. What's more, the reversal of the ferroelectric polarization can regulate the magnitude of MCA by several times, which demonstrates the efficient ferroelectric control on magnetism of AFM MnPt films. Remarkably, for the case of Pt-O interface, MnPt films significantly enhance perpendicular magnetic anisotropy (PMA) in comparison with the bulk $L1_0$-MnPt (MCA $=$ 0.176 meV/u.c., easy axis is along the c axis) [36] and the $P_\downarrow$ polarization yields a larger PMA than the $P_\uparrow$ polarization state. On the other hand, for the case of Mn-O interface, MCA is always negative for the investigated MnPt films under both polarization states of $BaTiO_3$, and the magnitude of MCA

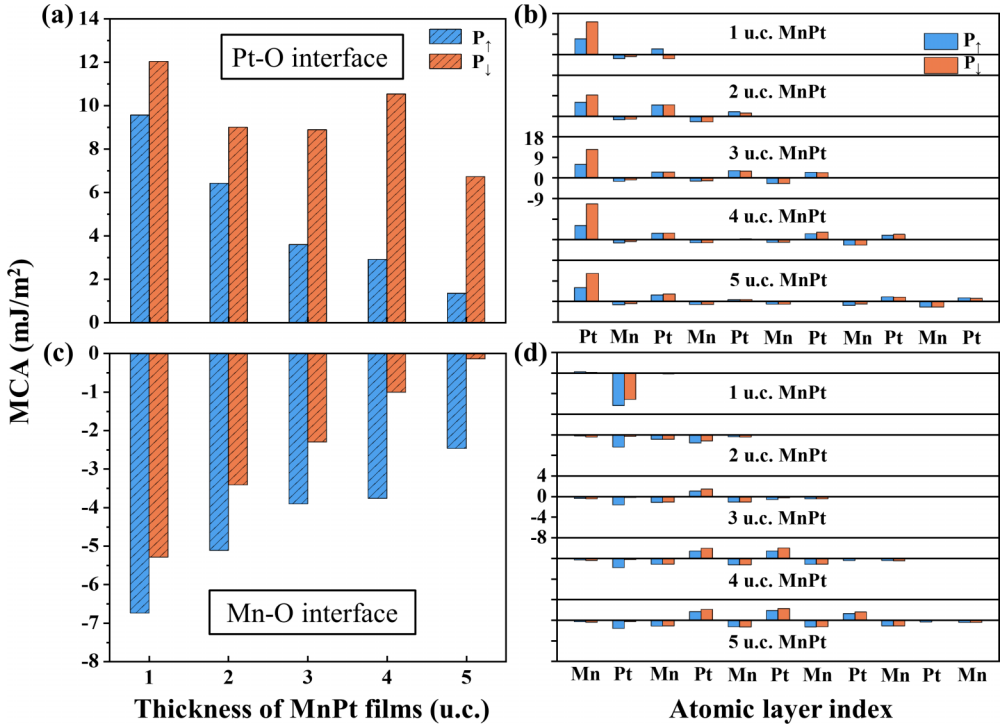

FIG. 2. Thickness dependence of MCA ($= E_{\text{band}}[100]$-$E_{\text{band}}[001]$) in MnPt/$BaTiO_3$ bilayers for $P_\uparrow$ (blue) and $P_\downarrow$ (orange) states for the cases of (a) Pt-O and (c) Mn-O interfaces. The layer-resolved MCA for the cases of (b) Pt-O and (d) Mn-O interfaces. Panels (b) and (d) have the same tick labels for MCA, and for simplicity, only tick labels for 3 u.c. MnPt films have been shown.

decreases monotonically as the thickness of MnPt layers increases [Fig. 2(c)]. In some simple cases, the MCA of films could be described by a model as $K = K_{\text{is}} + K_{\text{b}}^{*}t$, where K represents the total MCA of films, K_{is} represents the interface and surface MCA contributions and K_{b} is the bulk MCA, and t is the film thickness. Ideally, the MCA may show a linear dependence on the film thickness with a slope as the bulk MCA and the intercept as the surface/interface MCA contribution. However, this asymptotic behavior is not present in the studied MnPt films, possibly due to complicated thickness dependence of MCA on surface/interface contribution, or formation of quantum well states.

To gain more insight on MCA and the ferroelectric control of MCA, we could evaluate the layer resolved MCA by projecting the SOC energy (E_{SOC}) on each atom and taking the energy difference when the magnetization is along [100] and [001] directions. The MCA contribution thus can be reversed on each atomic layer as [37]

$$\text{MCA}^{i} \approx \tfrac{1}{2}\left(E^{i}_{\text{SOC}}[100] - E^{i}_{\text{SOC}}[001]\right), \tag{1}$$

where i represents atomic layer index and a positive MCA^{i} means that the atomic layer contributes positive MCA and tends to PMA.

For the Pt-O interface case, as it is shown in Fig. 2(b), the Pt layers contribute positive MCA and the interfacial Pt atomic layer contributes the largest MCA. The ferroelectric polarization reversal of $BaTiO_3$ significantly modifies the MCA on the interfacial Pt layer and therefore leads to ferroelectric control of total MCA in MnPt films. The mechanism for PMA (perpendicular magnetic anisotropy) and the ferroelectric control of MCA mechanism for Pt-O interface case can be attributed to orbital hybridization between Pt-5d and O-2p orbitals as we will discuss later. The crucial role of the interfacial Pt atoms on MCA and the polarization control of MCA is further revealed from Figs. 2(b) and 2(d), which is owing to the inherently large SOC constant ξ and induced magnetic moment on Pt (the magnetic moment on Pt is around 0.1 μ_{B} as it is shown in Appendix D). A similar significant MCA contribution from a nonmagnetic atom (or induced magnetic moment on nonmagnetic atoms) has been reported in previous literature [38–41].

For the case of the Mn-O interface, as it is shown in Fig. 2(d), the Pt atoms next to the Mn-O interface exhibit negative contribution to MCA and also show the modulation upon polarization reversal. As the MnPt thickness increases, the Pt atoms in the middle layer of MnPt films start to restore the bulklike feature, and start to contribute positive MCA. Consequently, the magnitude of negative MCA decreases monotonically as the thickness of MnPt layers increases as shown in Fig. 2(c). The in-plane MCA and its ferroelectric control of Néel vector can also be attributed to the change of electronic structure on Pt atomic layer nearest to the Mn-O interface as we will discuss later.

In the following, we will qualitatively analyze the origin of MCA and its ferroelectric polarization controlled effect in MnPt/$BaTiO_3$ bilayers based on the second order perturbation theory [42–44]. In perturbation theory, the spin-orbit coupling (SOC) Hamiltonian can be written as

$$H_{\text{soc}} = \xi(r)\vec{\sigma} \cdot \vec{L} \tag{2}$$

where $\overrightarrow{L}$ is the orbital angular momentum operator, $\overrightarrow{\sigma}$ is the Pauli matrix, and $\xi(r)$ is the atomic spin-orbit coupling strength. Generally, since SOC energy is at the order of tens of meV, it can be treated as energy perturbation. The second order energy correction due to SOC is related to the magnetization direction M_η and can be written as [42–45]

$$\Delta E_{\rm soc}(M_\eta) = \frac{\xi^2}{4}\sum_{\alpha,\beta}\sum_{o,u}\frac{\left|\left\langle\psi_o^\alpha\right|(\overrightarrow{\sigma}\cdot\overrightarrow{L})_{M_\eta}^{\alpha\beta}\left|\psi_u^\beta\right\rangle\right|^2}{\varepsilon_o^\alpha-\varepsilon_u^\beta}, \qquad (3)$$

where α, β are the spin indexes (α, $\beta = \uparrow, \downarrow$), ψ_o^α and ψ_u^β are the occupied (above Fermi energy) and unoccupied (below Fermi energy) wave functions in the absence of SOC, and ε_o^α and ε_u^β are the corresponding band eigenvalues.

The SOC Hamiltonian is shown in Eq. (2), and therefore, the energy correction $\Delta E_{\rm soc}(M_\eta)$ in Eq. (3) is related to the magnetization orientation (M_η) and, in consequence, leads to MCA. By integrating over $\boldsymbol{k}$ in the Brillouin zone, $\Delta E_{\rm soc}(M_\eta)$ can be approximately expressed by the product of the density of states (DOS) and the matrix elements of $\overrightarrow{\sigma}\cdot\overrightarrow{L}$ between a pair of d orbitals as follows [37,45]:

$$\Delta E_{\rm SOC}(M_\eta) = \frac{\xi^2}{4}\sum_{\mu,\mu'}P_{M_\eta}^{\alpha\beta}(d_\mu,d_{\mu'})\int_{-\infty}^{\varepsilon_F}d\varepsilon\int_{\varepsilon_F}^{\infty}\times d\varepsilon'\frac{\rho_\mu^\alpha(\varepsilon)\rho_{\mu'}^\beta(\varepsilon')}{\varepsilon-\varepsilon'};$$

$$P_{M_\eta}^{\alpha\beta}(d_\mu,d_{\mu'}) = \left|\langle d_\mu|(\overrightarrow{\sigma}\cdot\overrightarrow{L})_{M_\eta}^{\alpha\beta}|d_{\mu'}\rangle\right|^2 \qquad (4)$$

where d_μ belongs to one of the five d orbitals d_{xy}, d_{yz}, d_{xz}, $d_{x^2-y^2}$, and d_{z^2}. $\rho_\mu^\alpha(\varepsilon)$ is the density of states (DOS) for spin α and $\varepsilon_{\rm F}$ is the Fermi energy. The nonvanishing matrix element $(\overrightarrow{\sigma}\cdot\overrightarrow{L})_{M_\eta}^{\alpha\beta}$ between a pair of d orbitals will contribute to the SOC energy correction and favor the magnetization along the M_η direction. From the above perturbation analysis, one can realize that the MCA will be closely related to the nonvanishing matrix element $(\overrightarrow{\sigma}\cdot\overrightarrow{L})_{M_\eta}^{\alpha\beta}$ and the involved DOS distribution around the Fermi energy.

Hereafter, we will first analyze the MCA and its polarization regulation mechanism for Pt-O case by taking MnPt (4 u.c.)/$BaTiO_3$ as an example. Figures 3(a) and 3(b) show the d orbitals resolved MCA on interfacial Pt atomic layer for two polarization states in MnPt (4 u.c.)/$BaTiO_3$ bilayers. It clearly indicates that the orbital pair of (d_{z^2}, d_{yz}) contributes the largest positive MCA and such contribution has been significantly modulated upon ferroelectric polarization reversal from $P_\uparrow$ to $P_\downarrow$ state. By considering the fact that the Pt-O interface distance has been changed from 2.20 to 2.28 Å by polarization reversal from $P_\uparrow$ to $P_\downarrow$, one can infer that the control of MCA may be correlated to the modification of interface orbital hybridization.

Indeed, Figs. 3(c)–3(f) show the density of states (DOS) for Pt-5d and O-2p orbitals on Pt-O interface, which clearly indicate the orbital hybridization and the formation of bonding states between interfacial Pt and O atoms. This is evident from Figs. 3(c) and 3(e) that the interfacial Pt-d_{z^2} and O-p_z peaks have similar shapes and are located at the same position below Fermi energy. (Please note that the DOS of d_{xz} and d_{yz} orbitals do not degenerate on the interfacial Pt atom due to the x, y symmetry breaking at the interface.) On the other hand, based on the second order perturbation theory [37], for magnetic moment along the M_z direction ([001]), the nonvanishing matrix elements involved (d_{z^2}, d_{yz}) orbital pair are $\langle d_{yz}|(\overrightarrow{\sigma}\cdot\overrightarrow{L})_{M_z}^{\uparrow\downarrow}|d_{z^2}\rangle = -i\sqrt{3}$, while for the magnetic moment along the in-plane M_x direction, such a spin-flipped SOC matrix element is missing. In consequence, the presence of a d_{z^2} orbital around Fermi energy is essentially crucial for contributing to SOC energy correction $\Delta E_{\rm soc}(M_z)$ and thus favors positive MCA and resultant PMA.

The reduction of MCA from $P_\downarrow$ to $P_\uparrow$ polarization reversal can also be understood from the modification of orbital-resolved DOS, which is shown in Figs. 3(c) –3(f). Notably, the interfacial Pt-5d (mostly d_{z^2} and d_{yz}) and O-2p (mostly p_z and p_y) bonding states move simultaneously downward across the Fermi level through polarization reversal from $P_\downarrow$ to $P_\uparrow$. For the $P_\downarrow$ polarization state, the interface hybridization between the Pt-5d and O-2p orbitals leads to a larger d_{yz} and d_{z^2} DOS presented around Fermi energy than the case of $P_\uparrow$ polarization. Therefore, a larger contribution to positive MCA is contributed by the (d_{z^2}, d_{yz}) orbital pair for $P_\downarrow$ polarization. In order to further confirm the ferroelectric polarization reversal effect on the interfacial Pt layer, we also calculate the orbital projected band structure along high-symmetry lines as shown in Figs. 4(a) and 4(b). It is clear that when the ferroelectric polarization is reversed from $P_\downarrow$ to $P_\uparrow$, the d_{z^2} orbital contribution to energy bands around Γ points on interfacial Pt layer has been shifted below Fermi level.

By taking magnetic dipole-dipole anisotropy energy (M_{dd}) into account, the total MAE as a function of MnPt film thickness for Pt-O interface is shown in Fig. 7 in Appendix C. One can find that M_{dd} is positive and increases linearly for film thickness from 1 to 5 u.c. suggesting that the magnetic dipole-dipole energy favors the out-of-plane easy axis for AFM MnPt films. Therefore, in addition to MCA, the MAE ensures that the Néel vector of MnPt films with Pt-O interface always points along the out-of-plane [001] direction. The magnitude of MAE can be manipulated by several times through ferroelectric polarization reversal, which demonstrates the desired efficient ferroelectric control of MAE for AFM films.

In the following, we will qualitatively analyze the MCA and its polarization-controlled effect for the case of Mn-O interface. As previously shown in Fig. 2(c), for the Mn-O interface, the MCA of MnPt films favor the in-plane magnetic easy axis for both ferroelectric polarization states. This result can also be understood from the electronic structure of Pt atomic layer nearest to the Mn-O interface. Figures 5(a) and 5(b) show the d-orbital resolved MCA on the Pt layer nearest to the Mn-O interface in MnPt (4 u.c.)/$BaTiO_3$ bilayers. It is clear that now the orbital pairs of $(d_{x^2-y^2}, d_{xy})$ and (d_{xz}, d_{yz}) contribute prominent negative MCA (favor the in-plane easy axis). Based on the second order perturbation theory, for a magnetic moment along the M_x direction ([100]), the nonzero matrix elements involving $(d_{x^2-y^2}, d_{xy})$ and (d_{xz}, d_{yz}) orbital pairs are the spin-flipped terms $\langle d_{x^2-y^2}|(\overrightarrow{\sigma}\cdot\overrightarrow{L})_{M_x}^{\uparrow\downarrow}|d_{xy}\rangle = -2i$ and $\langle d_{xz}|(\overrightarrow{\sigma}\cdot\overrightarrow{L})_{M_x}^{\uparrow\downarrow}|d_{yz}\rangle = -i$, while for magnetic moment along the M_z direction, those matrix elements are vanishing. Therefore, the presence of $d_{x^2-y^2}$, d_{xy}, d_{yz}, and

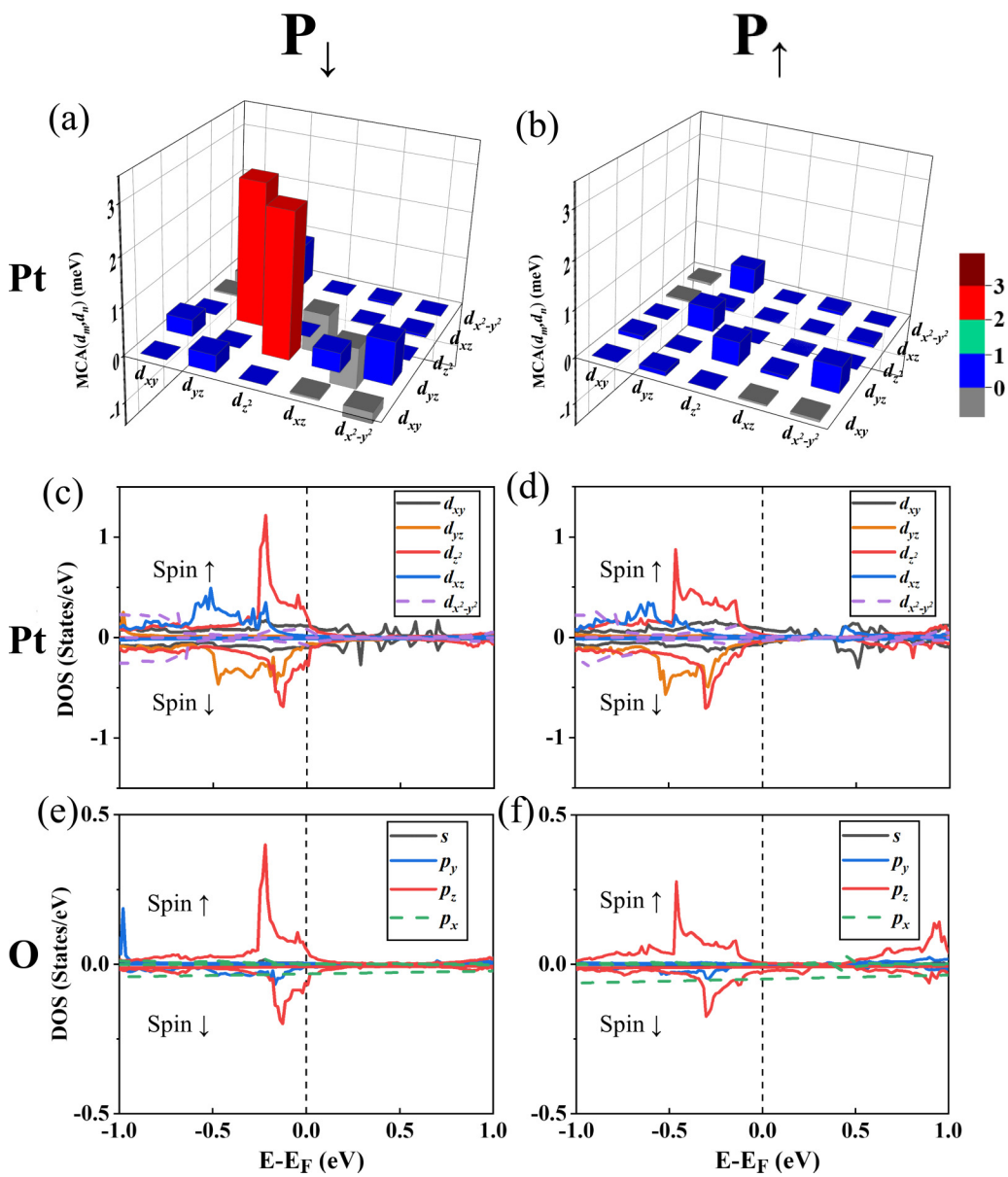

FIG. 3. The d-orbital resolved MCA on interfacial Pt atomic layer for $P_\downarrow$ (a) and $P_\uparrow$ (b) ferroelectric polarization states for the case of Pt-O interface in MnPt (4 u.c.)/$BaTiO_3$ bilayer. The orbital-resolved DOS on interfacial Pt and O atoms in MnPt (4 u.c.)/$BaTiO_3$ bilayers for $P_\downarrow$ and $P_\uparrow$; (c),(d) for Pt-5d orbitals; (e),(f) for O-2p orbitals. The Fermi level is set to zero.

d_{xz} orbitals around Fermi energy as shown in Figs. 5(c) and 5(d) could be partly responsible for negative MCA. On the other hand, in sharp contrast with the Pt-O interface, the missing of interface bonding between Pt-5d and O-2p orbital for the Mn-O interface case would reduce the positive MCA contribution by the (d_{z^2}, d_{yz}) orbital pair. In consequence, the MnPt films with Mn-O interface result in in-plane magnetic easy axis. As shown in Figs. 5(a) and 5(b), by reversing the polarization from $P_\downarrow$ to $P_\uparrow$, the main change of MCA on the Pt layer nearest to Mn-O interface is the (d_{yz}, $d_{x^2-y^2}$) orbital pair which has been changed from positive to negative MCA contribution.

The obvious redistribution of d-orbital occupation around Fermi energy occurs due to the polarization reversal as shown in Figs. 5(c) and 5(d). One can observe that the DOS around Fermi energy mainly include d_{z^2}, $d_{x^2-y^2}$, d_{yz}, and d_{xz} orbitals and the magnitude of DOS for such d orbitals decreases by reversing the ferroelectric polarization state from $P_\downarrow$ to $P_\uparrow$. There are similar d orbital pairs of nonzero matrix elements for SOC Hamiltonian H_{SOC} existing for magnetic moment (i.e., Néel vector) along the [100] and [110] directions [37]. And for such orbital pairs, the value of the SOC matrix element is different for those two in-plane magnetization orientations. For instance, for the orbital pair of (d_{xz}, $d_{x^2-y^2}$), for the [100] case the nonvanishing SOC matrix element is $\langle d_{xz}|(\vec{\sigma}\cdot\vec{L})^{\uparrow\downarrow}_{M_x}|d_{x^2-y^2}\rangle = -1$, while for the magnetic moment along the [110] direction it is $\langle d_{xz}|(\vec{\sigma}\cdot\vec{L})^{\uparrow\downarrow}_{M_{[110]}}|d_{x^2-y^2}\rangle = -\frac{\sqrt{2}}{2}$. Therefore, the reversal of ferroelectric polarization will modify the electronic structures

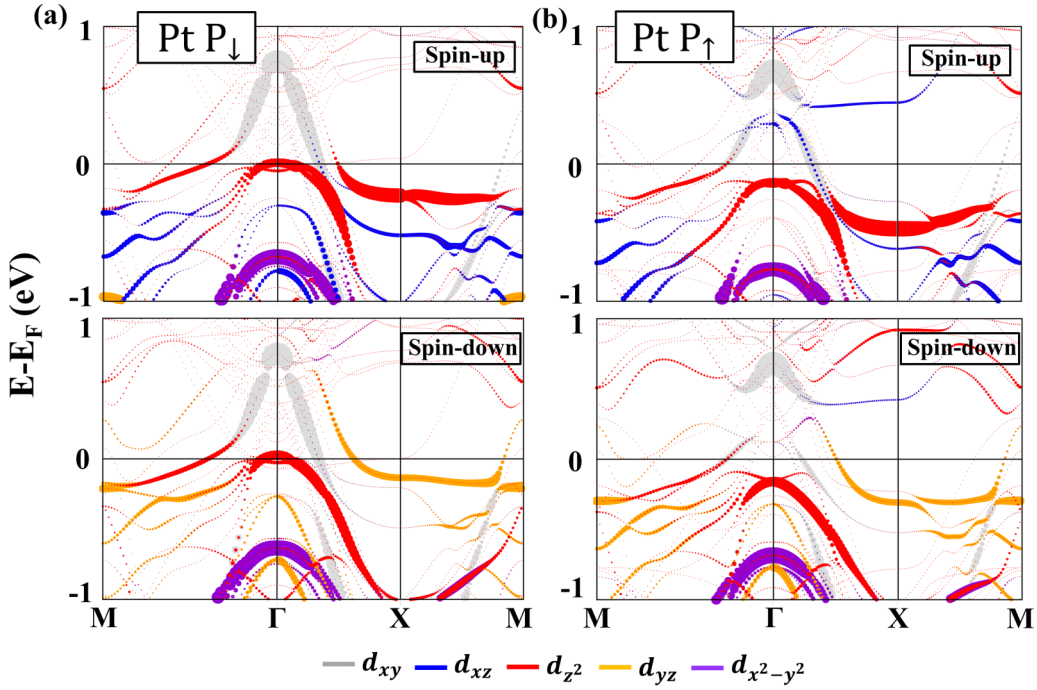

FIG. 4. The d-orbital (upper panels for spin up; lower panels for spin down) projected band structures on interfacial Pt atomic layer for $P_{\downarrow}$ (a) and $P_{\uparrow}$ (b) ferroelectric polarization states in MnPt (4 u.c.)/$BaTiO_3$ bilayers. The size of symbols represents the projected weight of different d orbitals. The Fermi level is set to zero.

and DOS around Fermi energy and thus change the relative SOC energy contribution for such orbital pairs for magnetic moment along the in-plane [100] and [110] directions. In consequence, it leads to the possible ferroelectric polarization driven switching between in-plane easy axes as we discuss below.

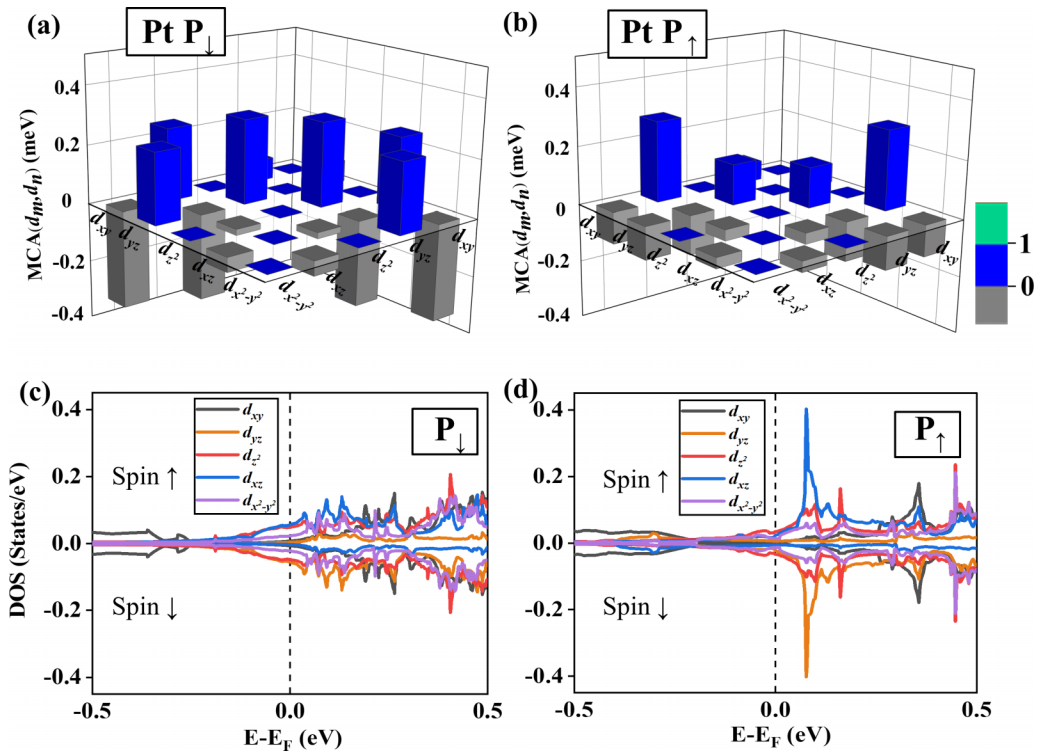

FIG. 5. The d-orbital resolved MCA on Pt atomic layer nearest to Mn-O interface for $P_{\downarrow}$ (a) and $P_{\uparrow}$ (b) ferroelectric polarization states for the case of Mn-O interface in MnPt (4 u.c.)/$BaTiO_3$ bilayer. And the corresponding d-orbital resolved density of states for $P_{\downarrow}$ (c) and $P_{\uparrow}$ (d) polarization states. The Fermi level is set to zero.

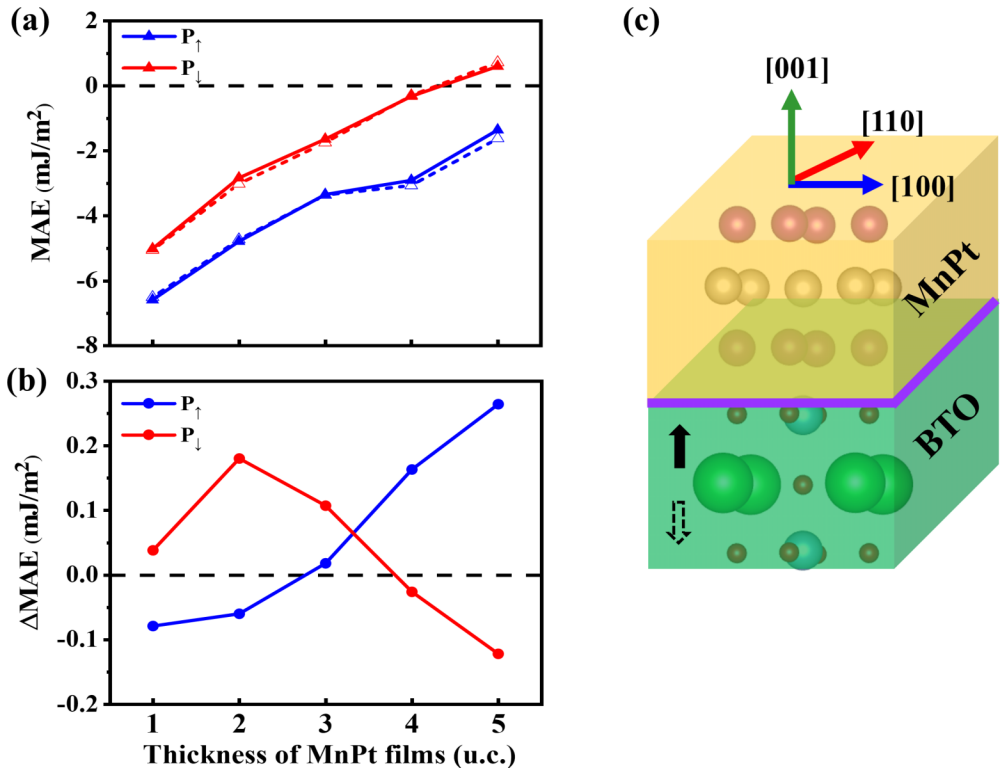

FIG. 6. (a) The calculated MAE (= $E[abc] - E[001]$, where $[abc]$ = [100] or [110]; the solid and dashed lines indicate MAE[100] and MAE[110], respectively) and (b) ΔMAE (= MAE[100]-MAE[110]) as a function of MnPt films thickness in MnPt/$BaTiO_3$ bilayer for Mn-O interface. The red and blue lines represent the MAE for $P_\downarrow$ and $P_\uparrow$ polarization states. (c)The illustration of ferroelectric control of Néel vector in MnPt films. The black arrows indicate the polarization direction of $BaTiO_3$ (BTO), and the blue, red, and green arrows represent Néel vector along in-plane [100], [110], or out-of-plane [001] directions, respectively.

By considering the total magnetic anisotropy contributed from MCA and magnetic dipole-dipole anisotropy energy M_{dd}, Fig. 6(a) depicts the calculated MAE as a function of MnPt films thickness in MnPt/$BaTiO_3$ bilayers with Mn-O interface. One can observe that by flipping the ferroelectric polarization from $P_\uparrow$ to $P_\downarrow$, the sign of MAE will be changed from negative to positive for 5 u.c. MnPt film, which indicates the Néel vector of MnPt films will be reorientated from the in-plane to the out-of-plane direction. When the thickness of MnPt films is less than 5 u.c., the Néel vector of MnPt keeps in plane. Figure 6(b) shows the MAE difference (ΔMAE = MAE[100]-MAE[110]; the positive ΔMAE means the Néel vector of MnPt favors the [110] direction, and vice versa) between in-plane [100] and [110] directions. The calculation results indicate that the Néel vector of MnPt film can be switched between in-plane [100] or [110] directions. For instance, for 1–2 u.c. MnPt films, by reversing the ferroelectric polarization from $P_\uparrow$ to $P_\downarrow$, the Néel vector will switch from the [100] to the [110] direction, while for 3 u.c. MnPt films the same polarization reversal will reorientate the Néel vector from the [110] to the [100] direction. The above discussed ferroelectric switching of the Néel vector of AFM films is a desired nonvolatile method for controlling AFM states by electric field.

In recent experiments, a large electric current density is needed to switch the easy axis between [110] and [100] directions in Mn_2Au films [12,19,20]. Here, we demonstrate that for designed AFM MnPt films, the manipulation of the Néel vector can be realized by polarization reversal of adjacent ferroelectric materials. Such manipulation on the AFM state is nonvolatile and more energy efficient in comparison with current-driven switching. The ferroelectric manipulation of AFM states should not be limited to the representative material MnPt films as we studied in this work, and this phenomenon should be quite general for other AFM/ferroelectric materials bilayer structures.

IV. SUMMARY

In summary, ferroelectric control of MCA on the $L1_0$ type of antiferromagnets MnPt films has been investigated by using first-principles calculations. We consider two possible interface configurations with $BaTiO_3$, namely Pt-O and Mn-O interfaces. For the case of Pt-O interface, there are giant PMA induced by the ferroelectric $BaTiO_3$ due to the rising of the d_{z^2} orbital by Pt-5d and O-2p interface bonding, while the MnPt films have in-plane MCA for the Mn-O case in the studied thickness rang (1–5 u.c.). Interestingly, for Mn-O interface, at a certain thickness of MnPt films, the Néel vector can be switched between in-plane [100] and [110] directions, or even reorientated from the in-plane to the out-of-plane direction by reversing the ferroelectric polarization of $BaTiO_3$. These calculation results may provide a concept of nonvolatile electric control of the Néel vector in antiferromagnets, which should

be appealing for the development of high-speed, high-density and low-power consumption antiferromagnets based memory devices.

ACKNOWLEDGMENTS

J.Z. acknowledges support from the National Natural Science Foundation of China (Grant No. 11704135). Computations were partly performed on the Platform for Data-Driven Computational Materials Discovery at the Songshan Lake Materials Laboratory, Dongguan, China. The authors thank Prof. Xiaohui Liu from the School of Physics, Shandong University for helpful discussions.

APPENDIX A: BINDING ENERGY WITH DIFFERENT INTERFACES FOR MnPt/$BaTiO_3$ BILAYERS

To gain insight into interface stability, we calculated the binding energy with Pt-O and Mn-O interfaces by taking MnPt (4 u.c.)/$BaTiO_3$ as an example (see Table I). From the calculation results, we can find that the interface binding energy of Mn-O interface is larger than Pt-O interface both for $P_\downarrow$ and $P_\uparrow$ polarization states which suggests Mn-O interface may be more energy stable in comparison to Pt-O interface. Regarding the surface stability, we notice that the modulation and contribution of MCA in MnPt/$BaTiO_3$ largely originates from the interface MnPt layers instead of surface MnPt layers. In consequence, one would expect similar conclusions by considering other possible surface terminations.

APPENDIX B: STABLE MAGNETIC STATES (FM OR AFM) AT MnPt/$BaTiO_3$ INTERFACES

We further analyzed the stable interface magnetic states (FM or AFM) by taking the MnPt (4 u.c.)/$BaTiO_3$ (4 u.c.)/$BaTiO_3$ as an example. We calculate the total energy of the bilayers by setting the interface MnPt layer as FM or AFM states (see Table II). The results indicate that the reversal of the polarization direction does not change the interfacial AFM states both for Mn-O and Pt-O interfaces structure.

APPENDIX C: MAGNETIC DIPOLE-DIPOLE ENERGY CONTRIBUTION TO MAE

The MAE includes contributions from MCA and magnetic dipole-dipole anisotropy energy (M_{dd}) [41,46]. We calculate M_{dd} (defined as the magnetic dipole energy difference by taking [001] as reference: $M_{dd} = E_{dd}[abc]$-$E_{dd}[001]$, where $[abc]$ indicates the direction of Néel vector). The Néel vector dependant magnetic dipole energy E_{dd} is calculated based on the following equation by direct summation in real space with cutoff radius of 800 Å [47]:

$$E_{dd} = \frac{\mu_0}{4\pi}\sum_{i<j}\frac{1}{r_{ij}^3}\left[\boldsymbol{m}_i\cdot\boldsymbol{m}_j - 3\frac{(\boldsymbol{r}_{ij}\cdot\boldsymbol{m}_i)(\boldsymbol{r}_{ij}\cdot\boldsymbol{m}_j)}{r_{ij}^2}\right],$$

where $\boldsymbol{m}_{i,j}$ are the magnetic moments on atomic sites i and j, $\boldsymbol{r}_{ij}$ is the vector pointing from i to j, and μ_0 is the permeability in vacuum.

The convergence criterion of M_{dd} was set to be 10^{-10} meV. Figure 7 depicts the MCA and the magnetic dipole-dipole anisotropy M_{dd} to MAE as a function of films thickness with Pt-O interface. One can observe that the magnetic dipole-dipole anisotropy energy M_{dd} depends linearly on film thickness both for $P_\downarrow$ and $P_\uparrow$ polarization states with the value from 0.12 to 0.71 mJ/m^2. The M_{dd} as a function of thickness for Mn-O interface shows similar behavior.

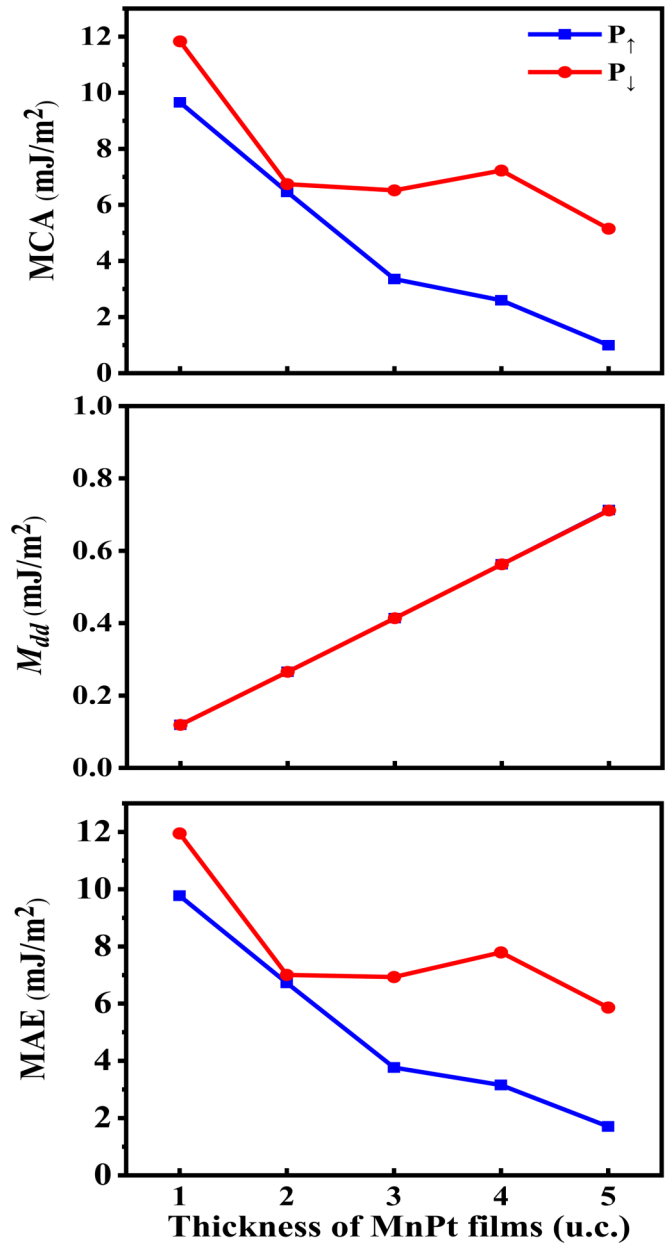

FIG. 7. MnPt thickness dependence of MCA, magnetic dipole-dipole anisotropy energy M_{dd} and the total MAE of MnPt/$BaTiO_3$ bilayers with Pt-O interface.

APPENDIX D: MAGNETIC MOMENTS ON Mn AND Pt ATOMS

By taking MnPt (2 u.c.)/$BaTiO_3$ and MnPt (4 u.c.)/$BaTiO_3$ as an example, we list magnetic moments of Mn and Pt atoms with two different interface structures in Table III. The induced magnetic moments on Pt atoms typically are around 0.1 μ_B.

TABLE I. The interface binding energy for Pt-O and Mn-O interface configurations, where E_0 (interface binding energy) $= E_0$ ($MnPt/BaTiO_3$) -E_0 (MnPt) -E_0 ($BaTiO_3$).

Interface Structure	Polarization direction	$E_0(MnPt/BaTiO_3)$ (eV)	E_0(MnPt) (eV)	$E_0(BaTiO_3)$ (eV)	Interface binding energy(eV)
Mn-O	$P_\uparrow$	−328.842 93	−142.473 10	−184.181 108	−2.189
	$P_\downarrow$	−328.718 05	−142.478 44	−183.637 820	−2.602
Pt-O	$P_\uparrow$	−323.441 53	−138.220 84	−183.980 770	−1.240
	$P_\downarrow$	−323.125 61	−138.240 23	−183.823 240	−1.062

TABLE II. Total energy for FM and AFM interface magnetic configurations. The energy differences between FM and AFM states are defined as $\Delta E = E_0$ (AFM) - E_0(FM).

Interface Structure	Polarization direction	E_0 (AFM) (eV)	E_0 (FM) (eV)	ΔE (eV)	Stable interface magnetic configurations
Mn-O	$P_\uparrow$	−328.842 93	−328.309 10	−0.534	AFM
	$P_\downarrow$	−328.718 05	−328.111 57	−0.606	AFM
Pt-O	$P_\uparrow$	−323.441 53	−322.864 83	−0.577	AFM
	$P_\downarrow$	−323.125 61	−322.590 67	−0.535	AFM

TABLE III. The magnetic moments of Mn atoms and the magnetically induced Pt atoms (μ_B) in the Mn-O interface and Pt-O interface configurations. Please note that for each layer there are two atoms.

		Interface layer		Middle layers					Surface layer	
Mn-O Interface		Mn	Pt	Mn	Pt	Mn	Pt	Mn	Pt	Mn
2 u.c. MnPt	$P_\uparrow$	−3.355	−0.058			−3.728			−0.072	−3.944
$BaTiO_3$		3.340	0.084			3.703			0.067	3.933
	$P_\downarrow$	−3.649	−0.089			−3.733			−0.069	−3.942
		3.571	0.062			3.703			0.069	3.945
4 u.c. MnPt	$P_\uparrow$	−3.354	−0.060	−3.706	−0.102	−3.705	−0.100	−3.717	−0.069	−3.926
		3.441	0.087	3.681	0.099	3.704	0.101	3.720	0.074	3.932
$BaTiO_3$	$P_\downarrow$	−3.671	−0.102	−3.704	−0.105	−3.709	−0.100	−3.719	−0.069	−3.928
		3.569	0.059	3.671	0.099	3.708	0.100	3.722	0.073	3.934
		Interface layer		Middle layers					Surface layer	
Pt-O Interface		Pt	Mn	Pt	Mn	Pt	Mn	Pt	Mn	Pt
2 u.c. MnPt	$P_\uparrow$	−0.091	−3.654			−0.111			−3.652	−0.102
		0.093	3.683			0.120			3.662	0.115
$BaTiO_3$	$P_\downarrow$	−0.087	−3.636			−0.107			−3.636	−0.111
		0.102	3.663			0.126			3.663	0.109
4 u.c. MnPt	$P_\uparrow$	−0.096	−3.644	−0.1	−3.703	−0.098	−3.714	−0.109	−3.658	−0.108
		0.090	3.663	0.117	3.723	0.104	3.711	0.109	3.655	0.106
$BaTiO_3$	$P_\downarrow$	−0.085	−3.607	−0.098	−3.713	−0.094	−3.711	−0.107	−3.659	−0.108
		0.104	3.663	0.117	3.723	0.106	3.712	0.110	3.657	0.106

[1] V. Baltz, A. Manchon, M. Tsoi, T. Moriyama, T. Ono, and Y. Tserkovnyak, Rev. Mod. Phys. **90**, 015005 (2018).

[2] T. Jungwirth, X. Marti, P. Wadley, and J. Wunderlich, Nat. Nanotechnol. **11**, 231 (2016).

[3] T. Jungwirth, J. Sinova, A. Manchon, X. Marti, J. Wunderlich, and C. Felser, Nat. Phys. **14**, 200 (2018).

[4] T. Shiino, S. H. Oh, P. M. Haney, S. W. Lee, G. Go, B. G. Park, and K. J. Lee, Phys. Rev. Lett. **117**, 087203 (2016).

[5] X. Marti, I. Fina, C. Frontera, J. Liu, P. Wadley, Q. He, R. J. Paull, J. D. Clarkson, J. Kudrnovsk, I. Turek, J. Kune, D. Yi, J. H. Chu, C. T. Nelson, L. You, E. Arenholz, S. Salahuddin, J. Fontcuberta, T. Jungwirth, and R. Ramesh, Nat. Mater. **13**, 367 (2014).

[6] P. Wadley, B. Howells, J. Železný, C. Andrews, V. Hills, R. P. Campion, V. Novák, K. Olejník, F. Maccherozzi, S. S. Dhesi, S. Y. Martin, T. Wagner, J. Wunderlich, F. Freimuth, Y. Mokrousov, J. Kuneš, and J. S. Chauhan, Science **351**, 587 (2016).

[7] A. Churikova, D. Bono, B. Neltner, A. Wittmann, L. Scipioni, A. Shepard, T. Newhouse-Illige, J. Greer, and G. S. D. Beach, Appl. Phys. Lett. **116**, 022410 (2020).

[8] C. C. Chiang, S. Y. Huang, D. Qu, P. H. Wu, and C. L. Chien, Phys. Rev. Lett. **123**, 227203 (2019).

[9] T. Hajiri, S. Ishino, K. Matsuura, and H. Asano, Appl. Phys. Lett. **115**, 052403 (2019).

[10] N. Bhattacharjee, A. A. Sapozhnik, S. Y. Bodnar, V. Y. Grigorev, S. Y. Agustsson, J. Cao, D. Dominko, M. Obergfell, O. Gomonay, J. Sinova, M. Kläui, H. J. Elmers, M. Jourdan, and J. Demsar, Phys. Rev. Lett. **120**, 237201 (2018).

[11] M. J. Grzybowski, P. Wadley, K. W. Edmonds, R. Beardsley, V. Hills, R. P. Campion, B. L. Gallagher, J. S. Chauhan, V. Novak, T. Jungwirth, F. Maccherozzi, and S. S. Dhesi, Phys. Rev. Lett. **118**, 057701 (2017).

[12] S. Y. Bodnar, L. Šmejkal, T. Jungwirth, O. Gomonay, A. A. Sapozhnik, H. J. Elmers, M. Kläui, and M. Jourdan, Nat. Commun. **9**, 348 (2018).

[13] T. Moriyama, K. Oda, T. Ohkochi, M. Kimata, and T. Ono, Sci. Rep. **8**, 14167 (2018).

[14] X. Z. Chen, R. Zarzuela, J. Zhang, C. Song, X. F. Zhou, G. Y. Shi, F. Li, H. A. Zhou, W. J. Jiang, F. Pan, and Y. Tserkovnyak, Phys. Rev. Lett. **120**, 207204 (2018).

[15] L. Baldrati, O. Gomonay, A. Ross, M. Filianina, R. Lebrun, R. Ramos, C. Leveille, F. Fuhrmann, T. R. Forrest, F. Maccherozzi, S. Valencia, F. Kronast, E. Saitoh, J. Sinova, and M. Kläui, Phys. Rev. Lett. **123**, 177201 (2019).

[16] S. DuttaGupta, A. Kurenkov, O. A. Tretiakov, G. Krishnaswamy, G. Sala, V. Krizakova, F. Maccherozzi, and S. Dhesi, Nat. Commun. **11**, 5715 (2020).

[17] Y. Cheng, S. Yu, M. Zhu, J. Hwang, and F. Yang, Phys. Rev. Lett. **124**, 027202 (2020).

[18] P. Zhang, J. Finley, T. Safi, and L. Liu, Phys. Rev. Lett. **123**, 247206 (2019).

[19] X. F. Zhou, X. Z. Chen, J. Zhang, F. Li, G. Y. Shi, Y. M. Sun, M. S. Saleem, Y. F. You, F. Pan, and C. Song, Phys. Rev. Appl. **11**, 054030 (2019).

[20] X. F. Zhou, J. Zhang, F. Li, X. Z. Chen, G. Y. Shi, Y. Z. Tan, Y. D. Gu, M. S. Saleem, H. Q. Wu, F. Pan, and C. Song, Phys. Rev. Appl. **9**, 054028 (2018).

[21] L. Q. Liu, O. J. Lee, T. J. Gudmundsen, D. C. Ralph, and R. A. Buhrman, Phys. Rev. Lett. **109**, 096602 (2012).

[22] H. Yan, Z. X. Feng, P. X. Qin, X. R. Zhou, H. X. Guo, X. N. Wang, H. Y. Chen, X. Zhang, H. J. Wu, C. Jiang, and Z. Liu, Adv. Mater. **32**, 1905603 (2020).

[23] C. Song, Y. F. You, X. Z. Chen, X. F. Zhou, Y. Y. Wang, and F. Pan, Nanotechnology. **29**, 112001 (2018).

[24] C. G. Duan, S. S. Jaswal, and E. Y. Tsymbal, Phys. Rev. Lett. **97**, 047201 (2006).

[25] D. Odkhuu, Phys. Rev. B **96**, 134402 (2017).

[26] R. O. Cherifi, V. Lvanovskaya, L. C. Phillips, A. Zobelli, I. C. Infante, and E. Iacquet, Nat. Mater. **13**, 345 (2014).

[27] R. Y. Umetsu, A. Sakuma, and K. Fukamichi, Appl. Phys. Lett. **89**, 052504 (2006).

[28] J. F. Wang, A. H. Gao, W. Z. Chen, X. D. Zhang, B. Zhou, and Z. Y. Jiang, J. Magn. Magn. Mater. **333**, 93 (2013).

[29] G. H. Kwei, A. C. Lawson, S. J. L. Billinge, and S. W. Cheong, J. Phys. Chem. **97**, 2368 (1993).

[30] P. E. Blöchl, Phys. Rev. B **50**, 17953 (1994).

[31] J. P. Perdew, K. Burke, and M. Ernzerhof, Phys. Rev. Lett. **77**, 3865 (1996).

[32] G. Kresse and J. Hafner, Phys. Rev. B **47**, 558 (1993).

[33] G. Gerra, A. K. Tagantsev, N. Setter, and K. Parlinski, Phys. Rev. Lett. **96**, 107603 (2006).

[34] J. Neugebauer and M. Scheffler, Phys. Rev. B **46**, 16067 (1992).

[35] S. Bornemann, J. Minr, J. Braun, D. Kdderitzsch, and H. Ebert, Solid State Commun. **152**, 85 (2012).

[36] Y. R. Su, M. Y. Li, J. Zhang, J. Hong, and L. You, J. Magn. Magn. Mater. **505**, 166758 (2020).

[37] Y. R. Su, J. Zhang, J. Hong, and L. You, J. Phys.: Condens. Matter. **32**, 454001 (2020).

[38] J. Kim, K.-W. Kim, B. Kim, C.-J. Kang, D. Shin, S.-H. Lee, B.-C. Min, and N. Park, Nano Lett. **20**, 929 (2020).

[39] J. L. Lado and J. Fernández-Rossier, 2D Mater. **4**, 35002 (2017).

[40] D. Odkhuu, Sci. Rep. **8**, 6900 (2018).

[41] P. H. Chang, W. Fang, T. Ozaki, and K. D. Belashchenko, Phys. Rev. Mater **5**, 054406 (2021).

[42] D. S. Wang, R. Q. Wu, and A. J. Freeman, Phys. Rev. B **47**, 14932 (1993).

[43] P. Bruno, Phys. Rev. B **39**, 865 (1989).

[44] G. Van der Laan, J. Phys.: Condens. Matter **10**, 3239 (1998).

[45] J. Zhang, P. V. Lukashev, S. S. Jaswal, and E. Y. Tsymbal, Phys. Rev. B **96**, 014435(2017).

[46] L. Szunyogh, B. Újfalussy, and P. Weinberger, Phys. Rev. B **51**, 9552 (1995).

[47] M. Woinska, J. Szczytko, A. Majhofer, J. Gosk, K. Dziatkowski, and A. Twardowski, Phys. Rev. B **88**, 144421 (2013).